Extended Silicic Volcanism in the Gruithuisen Region—Revisiting the Composition and Thermophysical Properties of Gruithuisen Domes on the Moon

Nandita Kumari[1] ⓘ, Timothy D. Glotch[1] ⓘ, Jean-Pierre Williams[2] ⓘ, Mark T. Sullivan[2], Shuai Li[3], Benjamin T. Greenhagen[4],
Dany Waller[4], Tyler Powell[4], Catherine M. Elder[5] ⓘ, Benjamin D. Byron[5] ⓘ, and Katherine A. Shirley[6]

[1] Department of Geosciences, Stony Brook University, Stony Brook, NY, USA
[2] Department of Earth, Planetary, and Space Sciences, University of California, Los Angeles, CA, USA
[3] University of Hawaii, Manoa, HI, USA
[4] Johns Hopkins University Applied Physics Laboratory, Laurel, MD, USA
[5] Jet Propulsion Laboratory, California Institute of Technology, Pasadena, CA, USA
[6] Department of Atmospheric, Oceanic, and Planetary Physics, University of Oxford, Oxford, UK

Abstract

The formation mechanisms, extent, and compositions of red spots on the lunar surface have intrigued the lunar community for decades. By identifying a new dome and another silicic crater in the highlands nearby, we find that the silicic volcanism in the Gruithuisen region extends beyond the three major domes. Our observations indicate that the Gruithuisen domes have low iron and titanium contents. They are enveloped by ejecta from surrounding regions and host silica-rich material excavated by the young craters consistent with previous work. Our boulder maps of the Gamma dome display a high boulder count and indicate that the Diviner rock abundance maps are only sensitive to boulders larger than ∼2 m. The H-parameter values are sensitive to presence of rocks and may be a better indicator of rocks at submeter scales. The Delta dome has gentle slopes, lower rock abundance, and one young crater, and it could serve as a safe and scientifically valuable site for landing and exploration of the domes and nearby region. The dome also displays anomalously high H-parameter in the same region as the crater, indicating the potential presence of pyroclastic materials. We observe up to 200 ppm of OH/H_2O on the domes and nearby mare despite the presence of a weak magnetic field to the south of Delta dome, further supporting the potential presence of pyroclastics in the region. This study could potentially aid in logistical and scientific decisions of the future NASA missions in the region.

Unified Astronomy Thesaurus concepts: Lunar composition (948); The Moon (1692); Volcanism (2174)

1. Introduction

The Procellarum KREEP terrane (PKT) located within mare region is rich in incompatible elements such as thorium (e.g., Haskin et al. 2000; Jolliff et al. 2000). UV and IR images of the full Moon acquired and processed (suppressed albedo variation and increase color variation) by Whitaker (1972) showed the presence of anomalously red spots, unlike the blue mare region in the PKT, and were suspected to be of different composition. The regolith samples from returned from the Apollo 11, 12, 14, 15, and 17 missions include granitic compositions (e.g., Roedder & Weiblen 1970; Anderson et al. 1972; Ryder et al. 1975; Meyer et al. 1996) that have been proposed to be candidate rocks resulting from non-mare silicic volcanism on the lunar surface, also known as "red spots." Granites on Earth are typically formed by (1) melting of metasedimentary rocks (Chappell & White 1974), (2) extreme crystallization of mantle magma or magma of similar composition in orogenic settings (e.g., Thornton & Tuttle 1960), (3) melting of anhydrous basalt along plate boundaries (Whitney 1988), and (4) basaltic underplating of silicic laccoliths or batholiths in anorogenic settings (Loiselle & Wones 1979; Whitney 1988). The absence of plate tectonics and crustal water on the lunar surface make the presence of silicic volcanism enigmatic. Two mechanisms—silicate liquid immiscibility (e.g., Ryder 1976; Jolliff 1991) and basaltic underplating

(Hagerty et al. 2006) have been proposed to account for the generation of granitic compositions on the Moon. However, the lack of absolute quantification of SiO_2 wt.% and the lack of samples from these regions have made it hard to understand the scale and contribution of these two mechanisms in their formation. For this work, we have focused on one such region, known as the Gruithuisen domes. The Gruithuisen region is comprised of three domes located in the northern portion of Oceanus Procellarum (Procellarum KREEP terrane) on the lunar near side (Figure 1). The Gamma dome (36.5°N, 319.2°E) stands ∼1.8 km above the surrounding mare, with a diameter of ∼20 km. To the northwest of Gamma is the Northwest (NW) dome, standing ∼1.2 km above the surrounding mare with a ∼6 km base diameter. The elliptical Delta dome (36.0°N, 320.4°E) is located to the southeast of Gamma, with a height of ∼1.8 km and major axial diameter of ∼30 km (Figure 1). The domes are located amidst flood basalt plains and are characterized by high albedos, steep slopes on the flanks with portions of the flanks containing sinuous ridges that may represent late-stage emplacement of flows, and fresh craters exposing the interiors of each of the Gamma and Delta domes (Whitaker 1972; Wagner et al. 2002; Ivanov et al. 2016). Stratigraphic sequencing and crater counting from previous studies suggest that the Delta and Gamma domes formed between ∼3.85 Ga and ∼3.7 Ga subsequent to the large impacts such as Orientale and Imbrium (e.g., Ivanov et al. 2016). The surrounding mare was erupted following the formation of these domes, with emplacement of the mare units occurring up to 2 Ga (Wagner et al. 2002; Ivanov et al. 2016).
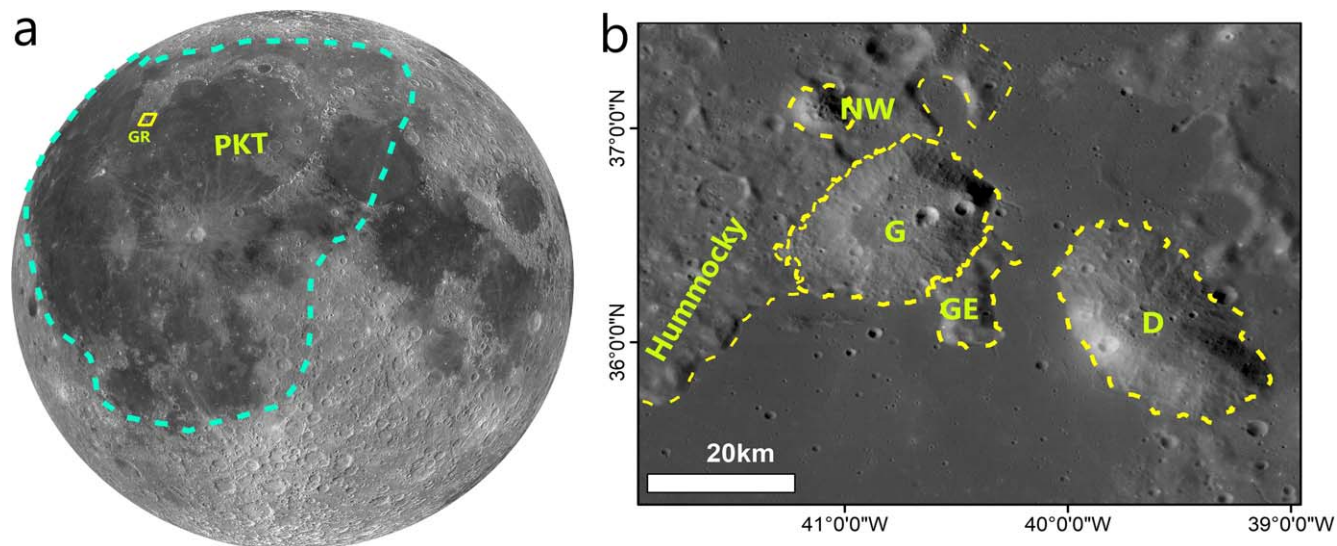
Figure 1. (a) Lunar Reconnaissance Orbiter Camera (LROC) Wide Angle Camera (WAC) image of Gruithuisen region displaying the near side of the Moon. PKT represents Procellarum KREEP Terrane and GR represents Gruithuisen Region. (b) Close-up view of the Gruithuisen region using WAC. G denotes Gamma dome, D represents Delta dome, NW indicates the Northwestern dome, GE denotes the Gamma Extension, and Hummocky denotes the highlands region nearby.

This work characterizes the compositional and thermophysical properties of the Gruithuisen domes region and uses the available data sets to condense the existing information from the remote sensing data sets available from several orbiting missions to provide important scientific context for the upcoming landed missions and future in situ observations, and perhaps to aid in mission planning.

1.1. Background

Several detailed investigations using remote sensing observations from different orbiters have been carried out to understand the composition of these domes. The domes are characterized as lunar red spots as a result of strong absorption in the ultraviolet (UV) (Whitaker 1972; Head & McCord 1978; Wagner et al. 2002). The visible–near-infrared (VNIR) analysis carried out using Clementine and the Moon Mineralogy Mapper (M^3) suggests that the domes are composed of non-mare material with low FeO and TiO_2 contents (e.g., Chevrel et al. 1999; Kusuma et al. 2012). Additional thermal IR (TIR) analysis carried out using the Diviner Lunar Radiometer Experiment (Diviner) aboard the Lunar Reconnaissance Orbiter (LRO) demonstrates that the domes have a short-wavelength Christiansen feature (CF) position, indicative of highly silicic compositions (Glotch et al. 2010). The Gamma and Delta domes also display free-air gravity anomalies indicating lower crustal densities (Kiefer et al. 2016) than the surrounding mare and highlands terrain. The gravity data suggest that the domes are likely made up of low-density and felsic material of vesicular or pyroclastic (or both) nature. The morphological properties and identified flow fronts along with the compositional analysis further indicates that these domes formed through extrusive volcanism (Wilson & Head 2003; Ivanov et al. 2016).

Non-mare lunar volcanism and samples of lunar granites are both relatively rare (e.g., Papike et al. 1998; Jolliff et al. 1999; Seddio et al. 2013, 2015; Yang et al. 2023). Because of their unusual occurrence and importance to understanding lunar volcanic history, the Gruithuisen domes region has been selected for two NASA Commercial Lunar Payloads Services

(CLPS) missions to further the scientific understanding and exploration of the Moon (NASA, 2022). The second Payloads and Research Investigations on the Surface of the Moon (PRISM) mission, the Lunar Vulkan Imaging and Spectroscopy Explorer (Lunar-VISE), will be delivered to the Moon in the time frame of 2026 (NASA, 2022). Lunar-VISE will land on the Gruithuisen Gamma dome with a suite of five instruments, three of which are mounted on the stationary lander and two on a mobile rover. VNIR and TIR multispectral cameras and a gamma-ray and neutron spectrometer (GRNS) will be mounted on the rover to map the compositional physical properties of the surface while the context and descent camera mounted on the lander will carry out landing site imaging and aid in understanding the interaction of lunar dust with the rover (Donaldson Hanna et al. 2023). The mission is currently planned to occur over one lunar day. In addition to this, another CLPS mission will land in the mare nearby the Gruithuisen domes in 2023 to maximize our scientific understanding of the region (Donaldson Hanna et al. 2023).

The lunar surface temperatures display high variation between day and nighttime due to the lack of an atmosphere, a thermally insulating surface layer of regolith, and slow rotation (e.g., Williams et al. 2017). The lack of atmosphere restricts the heat transfer within the lunar regolith through radiation amidst the pore spaces and conduction via grain-to-grain contact. This leads to the formation of a strong thermal gradient in the upper few cm of the lunar regolith, which depends on, and thus is indicative of, the packing style of the lunar regolith (e.g., Henderson & Jakosky 1997). Previous studies indicate that the thermal skin depth of the lunar surface varies from ~4 cm to 1 m between fine regolith and rocks on the lunar surface (e.g., Hayne et al. 2017). The thermal skin depth of a layer can be defined as the depth beyond which the temperature of the layer is not substantially affected by changes in diurnal or seasonal temperatures (i.e., the amplitude of the surface temperature oscillations has decayed to $1/e$). The temperature variation and thermophysical properties of the lunar regolith have been used to estimate the bulk grain size of the regolith at the CE-4 landing site (Xiao et al. 2022). An informed understanding through orbiter measurements can be

used to contextualize the future in situ measurements in the Gruithuisen region for similar results. This will also help unravel the compositions of the domes, narrow down the formation mechanisms of such domes, and improve our understanding of the thermal evolution of the Moon. In addition, temperature variation has also been used to distinguish different terrains on the lunar surface (Williams et al. 2022). Herein, we have used the bolometric temperature maps prepared using the day and nighttime measurements to understand the lateral and subsurface variation of the Gruithuisen domes region (Williams et al. 2022).

2. Data Sets and Methods

The FeO wt.% maps were created using Kaguya Multiband Imager (MI) images ($\sim$30 m px^{-1}) downloaded from the JAXA website and processed using the steps given in Lemelin et al. (2016). Diviner is a radiometer on board the Lunar Reconnaissance Orbiter with nine channels comprised of two solar channels and seven infrared channels. Channels 3, 4, and 5 are narrowband filters used to study the lunar composition corresponding to 7.55–8.05 μm, 8.1–8.4 μm, and 8.38–8.68 μm, respectively, while the remaining four channels, corresponding to $\sim$13–23, 25–41, 50–100, and 100–400 μm, respectively, are broadband channels that provide brightness temperature measurements that can be used to characterize the thermal properties of the regolith (Paige et al. 2009). The CF map (128 ppd) was prepared using Diviner channels 3, 4, and 5 constrained to local time coverage from 10 am to 2 pm (Paige et al. 2009; Greenhagen et al. 2010, 2011). The Kaguya FeO and Diviner CF maps help us to constrain the bulk compositions of features in the region and identify previously unmapped compositionally anomalous sites. The H-parameter from Hayne et al. (2017) and rock abundance map from Bandfield et al. (2011) and Bandfield et al. (2017), both derived from Diviner thermal measurements, were used to investigate thermophysical variations in the region. The H-parameter values are an indicator of thermal conductivity and density of regolith within the uppermost 10 s cm regolith depth, with lower H-parameter values indicating materials with higher density and thermal conductivity occur at shallower depths, and vice versa (Hayne et al. 2017). As a result, the H-parameter can be used as a proxy for thermal inertia at a given temperature and is inversely related to it. Thermal inertia is the ability of a material to conduct and store heat, and it is related to the bulk density and conductivity of the regolith, i.e., it is proportional to the square root of the product of the bulk density and conductivity. The thermal inertia of coarse grains and rocks is higher than that of fine-grained regolith. Thus, the H-parameter of coarse-grained regolith and rocks is lower than that of finer-grained regolith (Hayne et al. 2017). In addition to published Diviner rock abundance and H-parameter maps, we also generated Diviner temperature maps using the IR channels (3–9) at 0.25 hr local time intervals binned at 128 ppd (as described in Williams et al. 2017) and used these gridded data to derive products (e.g., maximum and minimum temperature maps) following the methods of Williams et al. (2022). We have then estimated the quartiles value of the temperature maps to understand the distribution of pixels displaying a range of temperatures. The temperature map and its derived products provide information about the thermophysical properties of the regolith, including the structure of the upper regolith and rock abundance, which can help us understand regolith evolution in the area and can also be useful to understand landing and roving hazards.

We calculated water abundances from Chandrayaan-1 M^3 data for all the optical periods covering the region (OP1A, OP1B, OP2B, and OP2C) at 1 km pixel^{-1} following the steps outlined in Li & Milliken (2017). We further used M^3 data to estimate 1 and 2 μm band centers to estimate mafic mineral composition in the area. For this, M^3 Optical Period 2C (OP2C) M^3 strips were georeferenced and mosaicked at their native resolution of 240 m px^{-1} for compositional maps. We then carried out continuum removal of 68 bands from $\sim$700 to $\sim$2576 nm. We spectrally subset the data cubes into two parts and carried out a parabolic fit to the data as described in Moriarty Iii & Pieters (2018). The estimated band centers (EBC1 and EBC2) were calculated by estimating the wavelength corresponding to the lowest value of the polynomial fit. The continuum-removed spectral band centers with band depths below 0.1 for the 1 μm feature were removed to prevent estimation of these parameters from noisy spectra. Lunar Prospector Magnetometer data with the highest spatial resolution at $\sim$3 km px^{-1} from Ravat et al. (2020) were used to identify and understand the magnetic field intensity in the region. The magnetic field strength decreases rapidly with distance from the source as a factor of $1/r^3$ for a dipole in free space, due to the inherent behavior of potential fields. These attenuations make it challenging for orbital data to accurately measure magnetic intensities and vector component strength at the surface (e.g., Richmond & Hood 2008; Purucker & Nicholas 2010; Tsunakawa et al. 2015; Ravat et al. 2020). As noted by Hemingway & Tikoo (2018), current inversion techniques can underestimate crustal field intensity by more than an order of magnitude. The surface magnetic field model used in this work should be treated as a lower bound on the magnetic intensity and used as a broader picture of regional field geometry.

The hyperspectral M^3 data set was used along with Kaguya data to ascertain the composition and to identify and quantify any water (OH/H$_2$O) in the region.

We mapped boulders using CraterTools (Kneissl et al. 2011) and high-resolution Lunar Reconnaissance Orbiter Camera (LROC) Narrow Angle Camera (NAC) images ($\sim$0.5–1 m px^{-1}) (Robinson et al. 2010). The images were selected using LROC Quickmap and processed using ISIS3, followed by manual co-registration with the global LROC Wide Angle Camera mosaic. The boulders were mapped by identification using their shadows and brighter pixel; coverage of at least two pixels was used as spatial constraint for mapping them. We have tried our best to also have each of the co-registered NAC images exactly atop one another and minimize the offsets to within $\sim$50 m. All the data sets used in this study and shapefiles will be available on Mendeley Data Repository. The boulder mapping was done to establish the sensitivity of Diviner rock abundance data set and identify hazardous regions in the area.

3. Composition—VNIR and TIR

We carried out a detailed compositional analysis of the entire Gruithuisen Domes region using VNIR M^3 and TIR Diviner data to understand the variation in composition across the region. Though the Gruithuisen domes have been known to display a lack of absorption at VNIR wavelengths (Kusuma et al. 2012), the mare area of Sinus Viscositatis surrounding the domes (target of the 2023 Astrobotic Peregrine-1 CLPS mission), has not been well characterized.
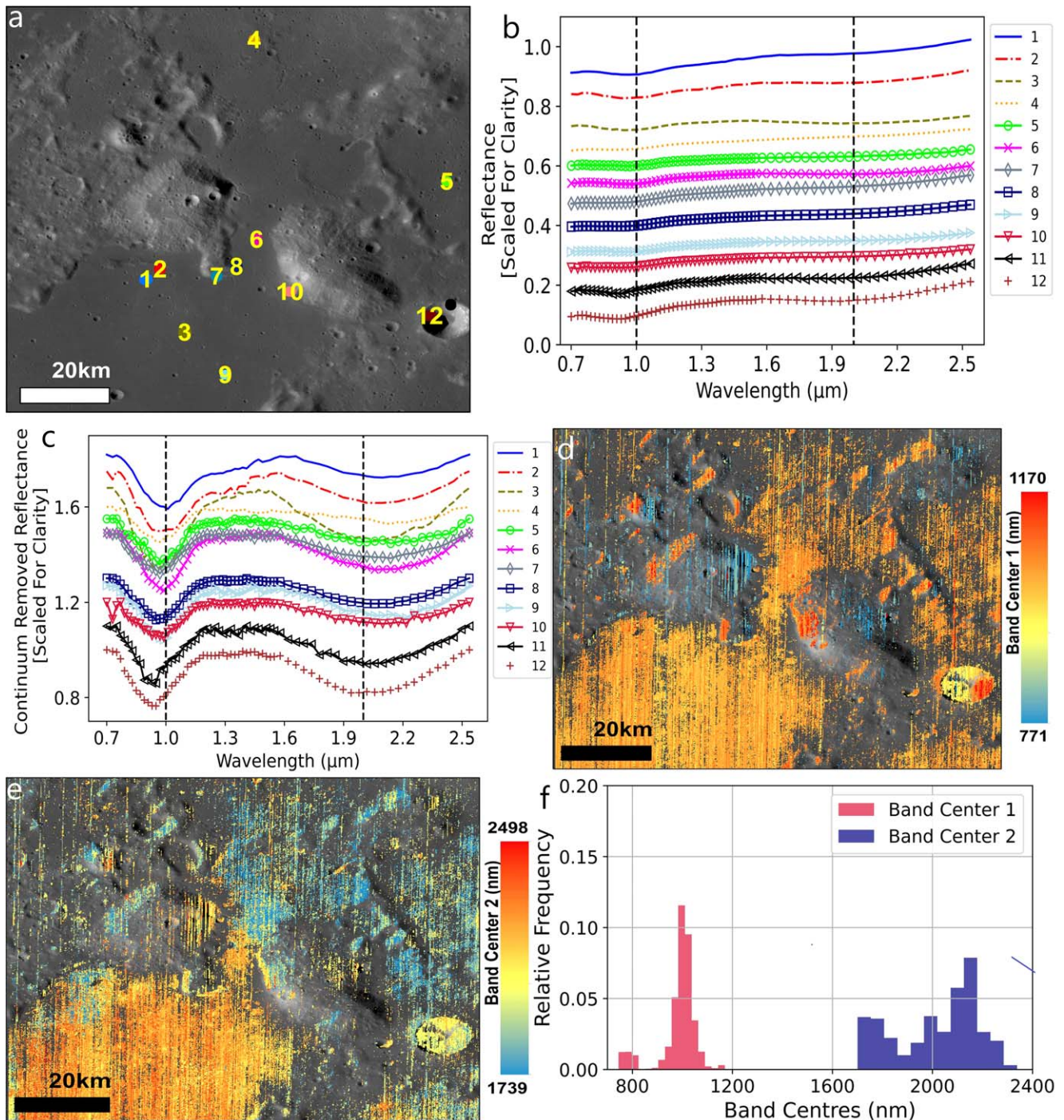
Figure 2. (a) WAC image of Gruithuisen domes region. (b) Reflectance spectra of the locations marked in 2a. The vertical lines represent 1000 and 2000 nm. (c) Continuum-removed reflectance spectra displayed in 2b. (d) M^3 map of estimated band center near 1000 nm (EBC1). (e) M^3 map of estimated band center near 2000 nm (EBC2). (f) Histogram displaying distribution of EBC1 and EBC2 over the region.

3.1. Moon Mineralogy Mapper (M^3)

The VNIR portion of the spectrum is highly sensitive to iron content, with pyroxene displaying two absorption bands near 1 and 2 μm, olivine with an absorption band near 1.05 μm, and plagioclase with a band near 1.25 μm (e.g., Cloutis 2002; Klima et al. 2007, 2008, 2011). The band center 1 (BC1) and band center 2 (BC2), corresponding to the two absorptions of pyroxene spectra near 1 and 2 μm, were estimated using the method described in Section 2. We extracted a few representative spectra with absorption depths more than 0.1 in the region

to understand the variation of mafic composition. The band center positions of the pyroxene spectra are indicative of the Fe–Mg–Ca content of the pyroxene (e.g., Cloutis 2002; Klima et al. 2007, 2008, 2011). As the band centers move toward longer wavelengths, the pyroxenes tend to be enriched in iron and calcium content (Klima et al. 2007, 2008, 2011).

We did not observe any spectra with defined absorption centers on the Gamma, Delta, Gamma Extension, or Northwest domes. In addition, we do not observe 1 μm or 2 μm bands in the hummocky highlands region to the west of the domes,
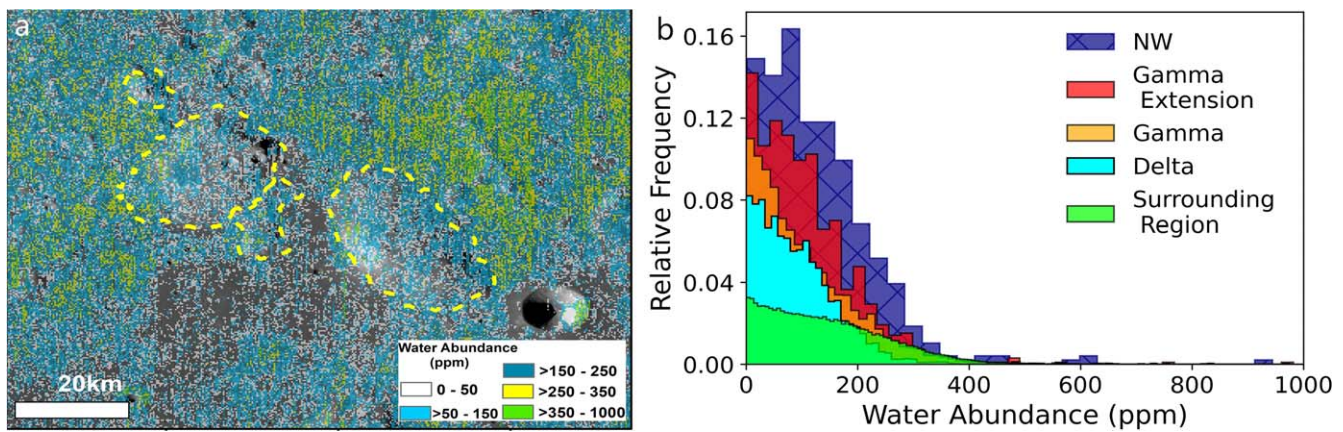
Figure 3. (a) Water abundance map of the region. (c) Histogram displaying the variation in water abundance over the three domes and surrounding region (includes both mare and highland shown in the figures).

despite the presence of small young craters in the region, indicating a lack of mafic material. Since most of the dome regions display featureless or noisy spectra (Figures 2(d)–(f)), we infer a lack of mafic minerals. Figures 2(b) and (c) display spectra with absorption near 1 and 2 μm, indicating the presence of pyroxene in the region. The region displays presence of both low-Ca and high-Ca spectra, with band centers below and above 0.95 μm, respectively. The histogram of the band centers shows that ~30% of the observed region with BC1 above 0.95 μm and BC2 above 2 μm corresponds to the presence of high-Ca pyroxene (Figure 2(d)). We observe that the extracted spectra also display band centers at longer wavelengths beyond 1 and 2 μm, confirming the presence of high-Ca pyroxene (Figures 2(d)–(f)). The presence of high-Ca pyroxene indicates the presence of evolved magmas. This, along with the late Imbrian- Eratosthenian ages computed by Ivanov et al. (2016), indicates that the mare regions most include magma rich in Fe and Mg but there also exist younger and magmatically evolved regions. We did not identify any pure anorthosite or olivine spectra in the region; however, we do observe an additional absorption band near 1.05 μm in some of the extracted spectra, which is usually caused by either the presence of glassy material, plagioclase, or olivine in the mixture (Klima et al. 2007, 2008, 2011) (Figure 2(c)).

In addition to the mineralogical analysis, we also used the 2.7 μm feature in the M^3 data to quantify any potential water in the region. The water abundance was estimated after carrying out a thermal correction (Li & Milliken 2017). The effective single-particle absorption-thickness (ESPAT) parameter was estimated by measuring absorption strength by converting the spectra to single scattering albedo. Though UV data acquired by the Lyman Alpha Mapping Project (LAMP) display H$_2$O mobility, they cannot distinguish between OH and structurally bound H$_2$O (Hendrix et al. 2019). This work assumes that the variation in H$_2$O observed at diurnal timescales can be caused solely by the formation and destruction of H-bearing species across the lunar surface causing variation in absorption depth. We find that the domes and the surrounding region host up to ~400 ppm water (Figures 3(a), (b)). The observed water content within the region is anomalously high relative to typical mare and highland regions and other red spots (Bhattacharya et al. 2015; Li & Milliken 2017; Milliken & Li 2017). The presence of water on and around the domes might indicate the presence of a water-rich magma source (e.g., Klima et al. 2011)

and/or felsic pyroclastic (e.g., Bhattacharya et al. 2015; Milliken & Li 2017) volcanism in the region.

3.2. Kaguya Multiband Imager and LRO Diviner

The Kaguya Multiband Imager (~30 m px^{-1}) was used to characterize the bulk chemistry and albedo of the region. The albedo values were extracted from 750 nm band of Kaguya MI data. The domes on average display higher albedo than the surrounding mare and highlands (Figure 4(a), Table 1). The NW and Gamma dome have the highest median albedo (~0.1) followed by the Delta dome (~0.09) (Figure 4(b), Table 1). The surrounding region median albedo is 0.07. The median albedo value (~0.09) (Figure 4(b)) of the Gamma extension is consistent with those of other domes. In addition, the 75th percentile value of surrounding region is also lower than the domes. The inclusion of pixels from young bright-rayed craters in the surrounding mare and the hummocky terrain are the probable reason for the lack of vastly different albedo values among the domes and the background. The sensitivity of Kaguya calibrated reflectance data within a band is less than 2% (Ohtake et al. 2008). We observe that the domes have higher albedo, compared to surrounding mare from the interquartile comparison, and they display higher reflectance. The region surrounding the domes has a median FeO of 14.41 wt.% (Figure 4(c), Table 1), while the Gamma extension has a median FeO of 11.28 wt.%. The median FeO abundances of the domes are: (1) 9.03 wt.% for the Gamma dome, (2) 10.63 wt.% for the Delta dome, and (3) 8.41 wt.% for the NW dome Figure 4(d), Table 1). The 5th percentile FeO wt% of the domes is 5.44 wt.% for Gamma, 7.65 wt.% for Delta, and 6.37 wt.% for NW—much lower than the surrounding region at 10.57 wt%. The Gamma dome displays the lowest iron content among the domes, probably due to the presence of young craters excavating and bringing the dome material to the surface as a consequence of stratigraphic inversion. This might indicate that internal material of the domes exposed on the surface of Gamma is the least contaminated compared to the other two domes. We also identified and carried out a detailed analysis of a small crater (~700 m diameter), hereby referred as New Crater (NC), and a mound, hereby referred as New Area (NA) in the hummocky region to the west of Gamma dome, which stood out with high albedo, low FeO content, and low CF value. The newly identified crater and mound display low FeO contents (5th percentile) of 5.6 wt% and 6.5 wt.%,
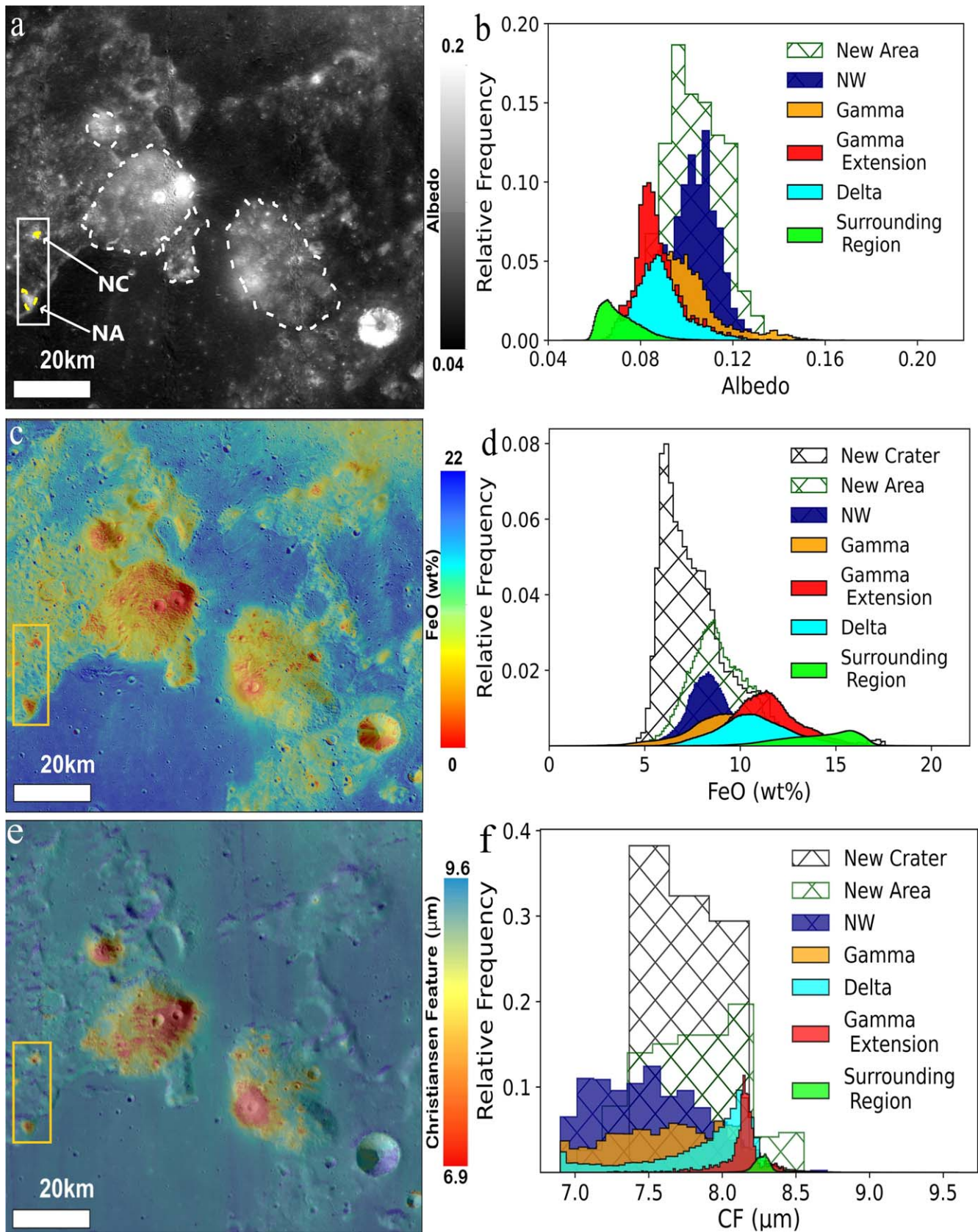
Figure 4. (a) Kaguya 750 nm image displaying the albedo of the region; NC and NA refer to the locations of the newly identified crater and mound. (b) Histogram displaying the variation in albedo of the three domes. (c) FeO image of the region. (d) Histogram displaying the variation in FeO wt.% of the three domes. (e) CF image of the region. (f) Histogram displaying the variation in CF of the three domes.

Table 1
FeO wt.% and Albedo Values of the Domes, Surrounding Regions, and Newly Discovered Areas

Name	FeO (wt.%) Percentile Values				Albedo Percentile Values				
	5th	25th	50th	99th	5th	25th	50th	75th	99th
Gamma	5.44	7.84	9.03	13.81	0.08	0.09	0.1	0.11	0.14
Delta	7.65	9.47	10.63	15.25	0.07	0.08	0.09	0.09	0.12
NW Gamma	6.37	7.65	8.41	11.51	0.08	0.1	0.1	0.11	0.12
Extension	8.64	10.22	11.28	15.78	0.07	0.08	0.09	0.09	0.12
Surrounding Region	10.57	12.78	14.41	17.26	0.06	0.06	0.07	0.08	0.11
NC	5.6	6.28	7.31	14.91	0.08	0.09	0.1	0.11	0.12
NA	6.51	7.78	8.67	11.6	0.09	0.1	0.1	0.11	0.13

Table 2
CF Values of the Domes, Surrounding Regions and Newly Discovered Areas

Name	CF (μm) Percentile Values			
	5th	25th	50th	99th
Gamma	6.99	7.33	7.65	8.41
Delta	7.04	7.71	8.0	8.41
NW	7.0	7.2	7.47	8.27
Gamma Extension	7.82	8.1	8.15	8.41
Surrounding Region	8.16	8.23	8.27	8.56
NC	7.38	7.49	7.77	8.15
NA	7.25	7.55	7.8	8.46

respectively. The FeO wt.% calculation formula uses an angular value between 950 nm/750 nm and 750 nm reflectance with an optimized origin estimated without any highly felsic samples, so the values for the domes might not be entirely accurate (Lucey et al. 2000). Hence, we can only infer that the domes are felsic in nature, based on the FeO wt.% data alone. The higher iron abundances that we observe on the tops of the Gamma and Delta domes are probably from the ejecta blanketing their surfaces from the craters in the surrounding mare (Figures 4(d) and (f)). The two young craters excavating the Gamma and Delta domes display lower iron content, indicating that the domes themselves are made up of more felsic material.

Diviner CF values for the Gruithuisen Domes display a range from ∼7 to 8.8 μm (Table 2). The 5th percentile of the CF values observed at Gamma (6.99 μm), Delta (7.04 μm), and NW (7.0 μm) are much lower than those of the surrounding region (8.16 μm), indicating felsic composition of the domes, while the Gamma extension displays the CF at 7.82 μm. The young craters atop the Gamma and Delta domes display CF values below 7.5 μm, indicating the presence of highly silicic material (Figure 4(f)) (e.g., Glotch et al. 2010; Greenhagen et al. 2010; Ivanov et al. 2016; Kiefer et al. 2016).

We observe that the newly identified crater displays bright rays (Figures 5(a) and (b)) and high median albedo (0.1, see Table 1), indicating that the crater is young and likely formed during the Copernican period. In addition, we also find that both the young crater and the mound in the hummocky highlands region (region within the yellow rectangle in Figures 4(a), (c), and (e)) to the west of the domes display high median albedos of 0.1, comparable to those of Gruithuisen domes. We also observe that all the smaller craters in the region display lower FeO abundances and shorter-wavelength CF positions (Figures 5(a)–(d)).

The crater and the mound are characterized in detail in Figure 5(a). The crater is a relatively young impact crater of diameter ∼700 m within an existing crater (Figures 5(a) and (b)) of diameter ∼2.1 km. The young crater displays lower FeO abundance (5th percentile of 5.6 wt% and median of 7.3 wt.%) and shorter-wavelength CF position (5th percentile of 7.38 μm; median of 7.77 μm) (Figures 5(c) and (d), Tables 1 and 2) compared to the surrounding terrain, whereas the 5th percentile and median of FeO abundance of the mound lie at 6.51 wt.% and 8.68 wt.%, while the CF positions lie at 7.25 μm (5th percentile), with the median at 7.8 μm (Figures 5(c)–(d)). The albedo, iron abundances, and CF values of the newly identified mound and crater are akin to those from the young crater ejecta atop the domes. These values are also much lower (<7.4 μm) than the typical CF values (∼7.8 μm) of highland material (Greenhagen et al. 2010), and along with lower and highland comparable FeO values (<7 wt.%), they indicate that this is not a massif of the Imbrium basin. This might indicate that these regions have similarly silicic compositions. Topographically, the mound has a height of ∼900 m above the surrounding mare (Figure 5(e)) and stands ∼500 m above the nearby highlands, which might indicate it to be a small dome.

The detailed spectral analysis of the region revealed that the region is composed of basaltic lava and silicic materials make up the domes. While this is useful to identify diverse compositional locations for sampling, the thermal analysis of the surface using temperature and its derived products, such as the H-parameter (Hayne et al. 2017), can help us understand the thermophysical properties of the surface (Bandfield et al. 2011; Williams et al. 2017, 2022). The thermophysical properties of the surface can be used to identify rocks for sampling as well as landing and roving hazards due to high density of rocks in a region.

4. Thermophysical Properties

4.1. Temperatures

The nighttime temperature of the surface is sensitive to the thermal inertia of the surface. Thermal inertia is the property of a material to retain heat and is defined as the square root of the product of thermal conductivity, density of the material, and specific heat capacity of the material. For instance, regolith has lower thermal inertia than rocks and thus heats up very quickly during the daytime and appears cooler in the nighttime temperature maps, while the boulders display elevated temperatures because of high thermal inertia (Bandfield et al. 2011). The gridded Diviner temperature data were used to generate bolometric temperature maps of each hour of local time. A detailed analysis of the 24-hourly temperature maps of the region confirms that the temperatures for pixels with ⩽15° slope estimated using ∼240 m px^{-1} Lunar Orbiter Laser Altimeter (LOLA) data (hereby referred as flat surfaces)
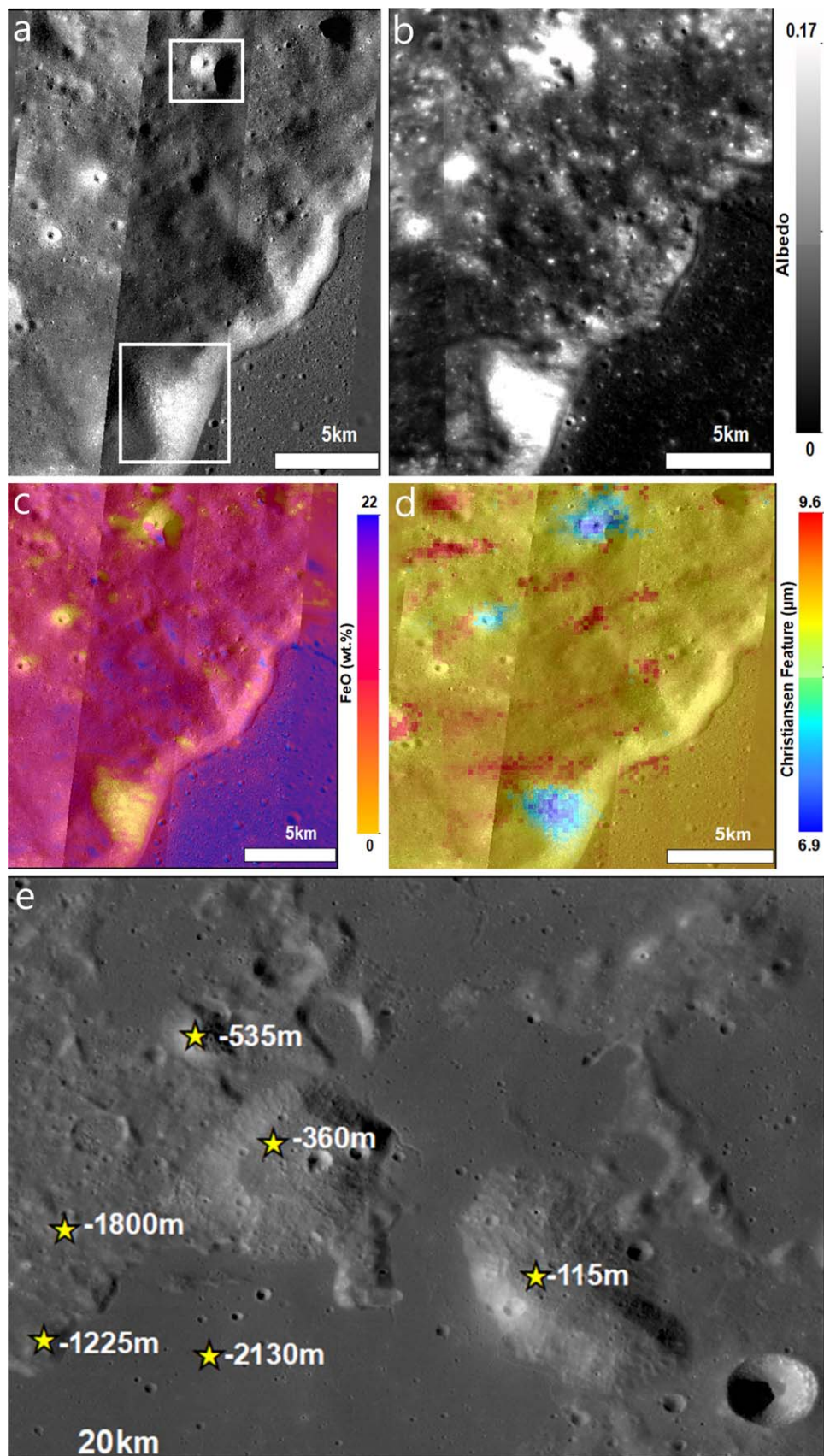
Figure 5. (a) NAC image of the hummocky region with the newly identified mound and the crater. (b) Kaguya 750 nm albedo image of region. (c) FeO image of the region. (d) CF image of the region. (e) Elevation of the domes and newly identified silicic regions overlaid onto the WAC image.
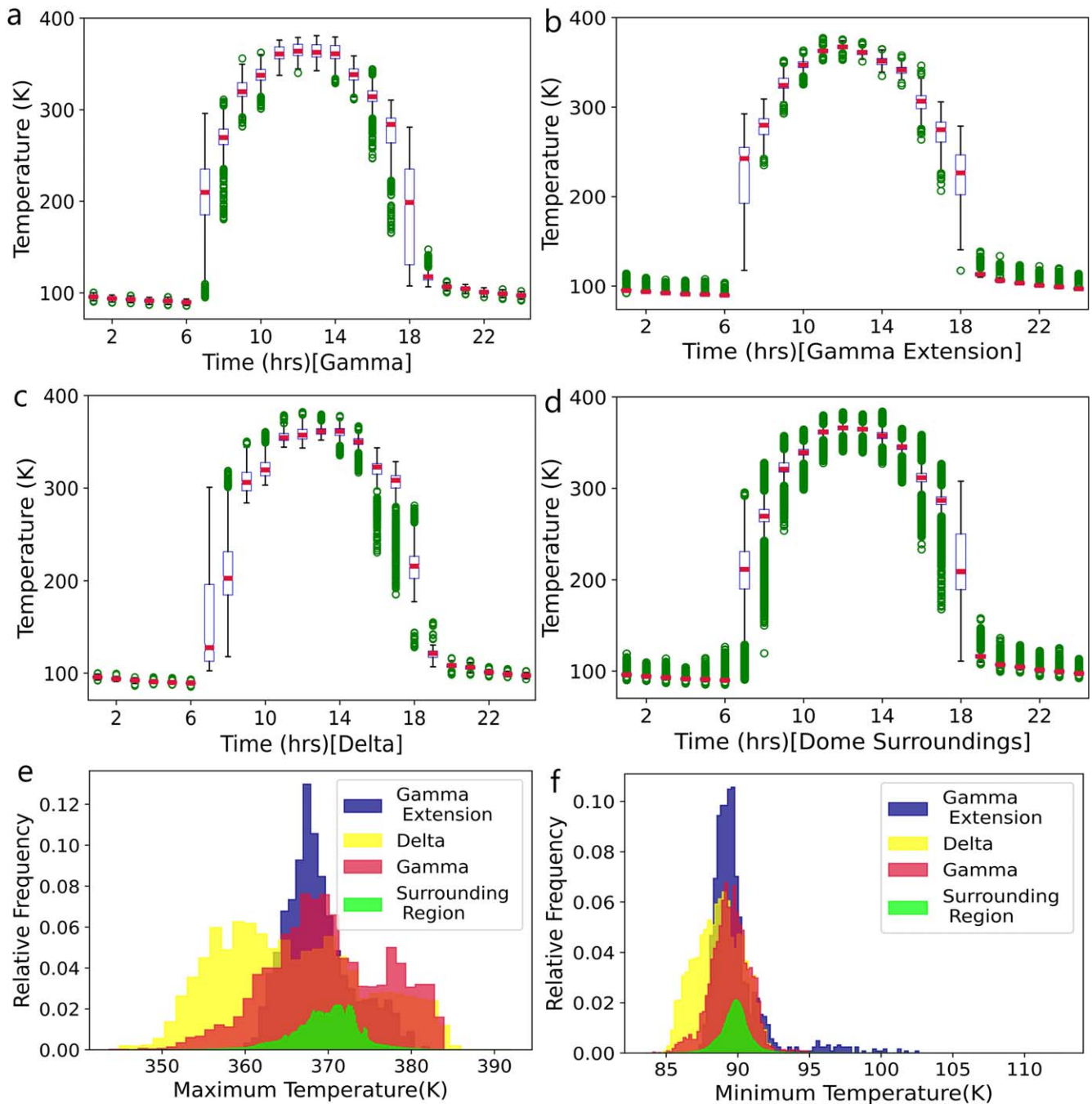
Figure 6. (a) 24 hr temperature variation of the Gamma dome. The beginning and end of the blue box represent the 25th and 75th percentiles of the values, and the pink line in the middle represents the 50th percentile (median). The black lines (or black dots) at the top and bottom are the maximum and minimum. The green dots are outliers with more than 1.5 times the value of the 25th or 75th percentiles. (b) 24 hr temperature variation of the Gamma extension. (c) 24 hr temperature variation of the Delta dome. (d) 24 hr temperature variation of the mare and highlands area surrounding the domes. (e) Histogram displaying variation in the maximum temperature. (f) Histogram displaying variation in the minimum temperature. The data displayed for all the units in this figure are for flat surfaces. See Table A1 for more details.

generally reach maximum temperatures ∼375–380 K during midday (between ∼11am and ∼1pm local time) (Figures 6(a)–(d), Table A1 in the Appendix). The early morning and late afternoon local times see a large variation of temperatures, likely due to slopes and shadows, with the nighttime temperatures becoming more uniform as the surfaces cool during the lunar night (Figures 6(a)–(d)).

We also plotted the maximum and minimum temperatures of the flat surfaces of the domes and the surrounding region from the 24 hr temperature maps. Our observations indicate that the hummocky highlands and flat areas within the basaltic lava flows surrounding the domes display median noon temperatures in the range of ∼370 K, while the Gamma, Gamma extension, and Delta dome temperatures lie at ∼369 K, 365 K, and 368 K, respectively (Figures 6(e) and (f), Table 3). The percentile analysis of the maximum temperatures shows that the surrounding region consistently displays higher temperatures compared to the domes (Table 3). The higher noon
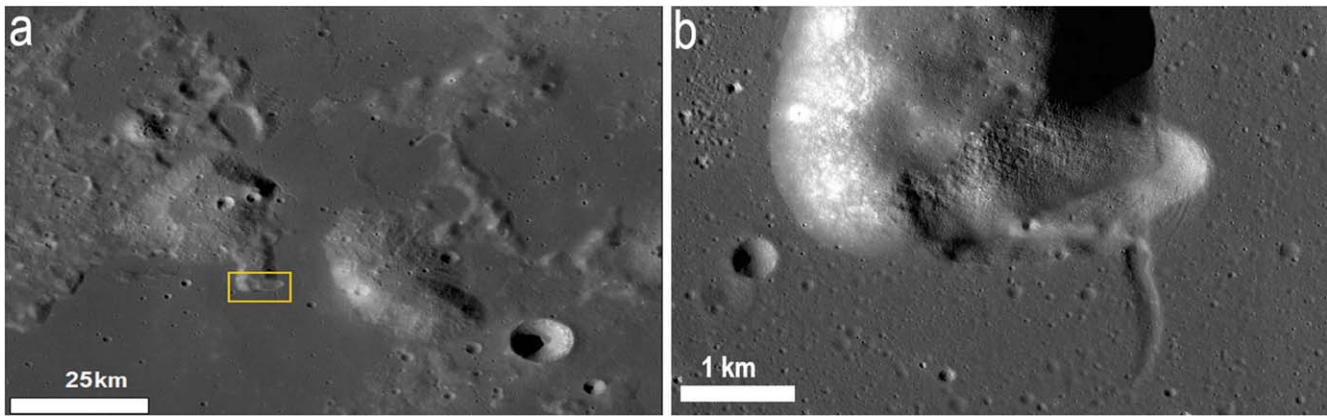
Figure 7. (a) Vent structure to the south of the Gamma extension. (b) High-resolution NAC view of the vent.

Table 3
24 hr Minimum and Maximum Temperatures of the Domes and Surrounding Regions

Name	Minimum Temperature (K) Percentile Values				Maximum Temperature (K) Percentile Values			
	5th	25th	50th	99th	5th	25th	50th	99th
Gamma	87.28	88.66	89.48	92.76	358.37	365.14	369	383.05
Delta	86.02	87.47	88.71	91.89	353.01	358.76	364.7	383.44
Gamma Extension	88.14	88.79	89.43	98.26	363.14	366.03	368	379.37
Surrounding Region	88.11	89.25	89.83	93.14	362.65	367.58	370	392.1

temperatures of the surrounding region can be attributed to lower albedo (Figures 4(a) and (b)), resulting in increased heating of the surface during the daytime.

The extended tail of the Gamma extension to warm nighttime temperatures (Figure 6(b)) indicates the presence of high thermal inertia material (Bandfield et al. 2011; Williams et al. 2017, 2022). This could be due to the vent-like structure in the south (Figures 7(a) and (b)) consisting of high thermal inertia materials such as boulders. The vent also appears warm in the minimum temperature map (Figure 8(f)) and the extension itself looks much more like the rest of the Gamma dome.

Topography, latitudinal variation, albedo, and thermophysical properties of the materials all contribute to variations in observed temperatures (e.g., Williams et al. 2017, 2022). The Gamma and Delta domes display a nonuniform distribution in the maximum temperature histogram (Figure 6(e)) compared with the minimum temperatures, which do not display a wide variation in temperatures among the different regions. The minimum temperatures of the region are predominantly affected by the thermophysical properties of the regolith, while the maximum temperatures are much more sensitive to the albedo and slope effects. For example, topography leads to variations in incidence angle that cause lateral variations in surface heating, i.e., an increase or decrease in heating of slopes facing toward or away from the Sun (Figure 8(a)).

We have normalized the maximum and minimum temperature maps of the area via a cosine fit between the mean temperature and latitude to remove the latitudinal gradient and highlight variations in temperature around the mean (Figures 8(b) and (e)). The darker vertical striping in Figure 8(c) results from areas that have incomplete coverage during midday when peak temperatures occur. The remaining temperature variations are largely dominated by the north–south slopes (Figure 8(c)). The influence of topography on the minimum temperatures is also apparent, but variations in temperature are largely due to variations in thermophysical properties (Figure 8(f)).

4.2. Thermal Inertia and Rock Abundance

Spectral anisothermality in a scene can be used to identify the presence of materials with distinct thermophysical properties (e.g., Bandfield et al. 2011; Williams et al. 2017, 2022). Here, we have used the difference between the maximum and minimum temperatures (i.e., the temperature amplitude) and the difference between the nighttime brightness temperatures estimated by Diviner channels 6 and 8 to identify different material properties. The regolith responds more rapidly to changes in illumination than rocks do, owing to its relatively lower thermal inertia. As a result, the regolith will heat up more quickly in the morning and cool more rapidly in the afternoon and evening, relative to rocks. Thus, lower thermal inertia materials can experience larger temperature amplitudes, though this will also depend on surface albedo. As a result, mixtures of low and high thermal inertia materials within a Diviner surface footprint will result in larger differences in nighttime temperatures between the Diviner channels 6 and 8 (i.e., greater anisothermality). Figure 9(a) shows that the regions with high normalized maximum temperatures and larger temperature change amplitudes in the image contain less high thermal inertia materials (i.e., have lower anisothermality) than those with lower normalized temperatures, after excluding slopes above 15° (Figure 9(b)). This indicates that these regions (pixels) host smaller amounts of compact material such as boulders. The H-parameter map (Figure 9(c)) shows that that the median H-parameter of the domes is higher than that of the
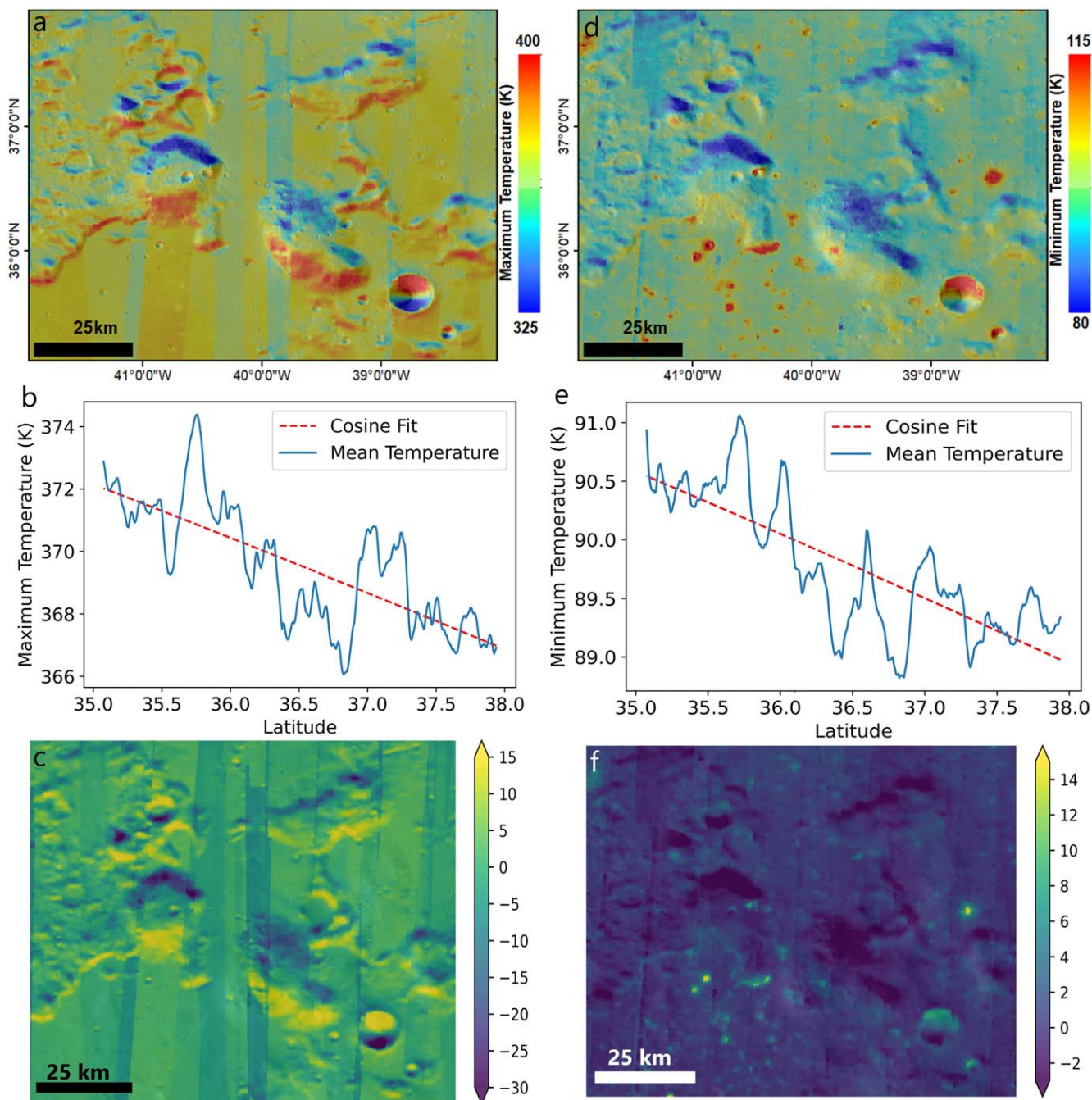
Figure 8. (a) Maximum temperature image of the region. (b) Cosine fit of the mean of the maximum temperatures by latitude. (c) Normalized maximum temperature of the region using the cosine fit from (b). (d) Minimum temperature image of the region. (e) Cosine fit of the mean of the minimum temperatures by latitude. (f) Normalized minimum temperature of the region using the cosine fit from (e).

nearby mare by 0.01 (Table 4). The histogram (Figure 9(d)) also displays that the H-parameter of the domes is higher than that of the mare, in line with the observations by Byron et al. (2023). Higher H-parameter indicates presence of fine-grained material on the site with lower compactness and thermal inertia. The southern slope of the Delta dome displays an anomalously high H-parameter despite the presence of a young crater on the surface and higher nighttime temperatures, indicating the presence of consolidated material or small boulders. Typically, higher H-parameter values are correlated with lower thermal inertia materials that have lower nighttime surface temperatures. The contrast in the observation via H-parameter

indicating low thermal inertia material while nighttime temperatures indicate the presence of boulders at the southern flanks of Delta dome can be explained by presence of glassy or vesicular pyroclastic material in the region. The lower bulk density of glassy or vesicular pyroclastic material results in lower thermal inertia and thus higher H-parameter, despite them being compact. This observation is in line with the observations made by Byron et al. (2023) who also noted higher H-parameter and increased rock abundance on the Delta dome.

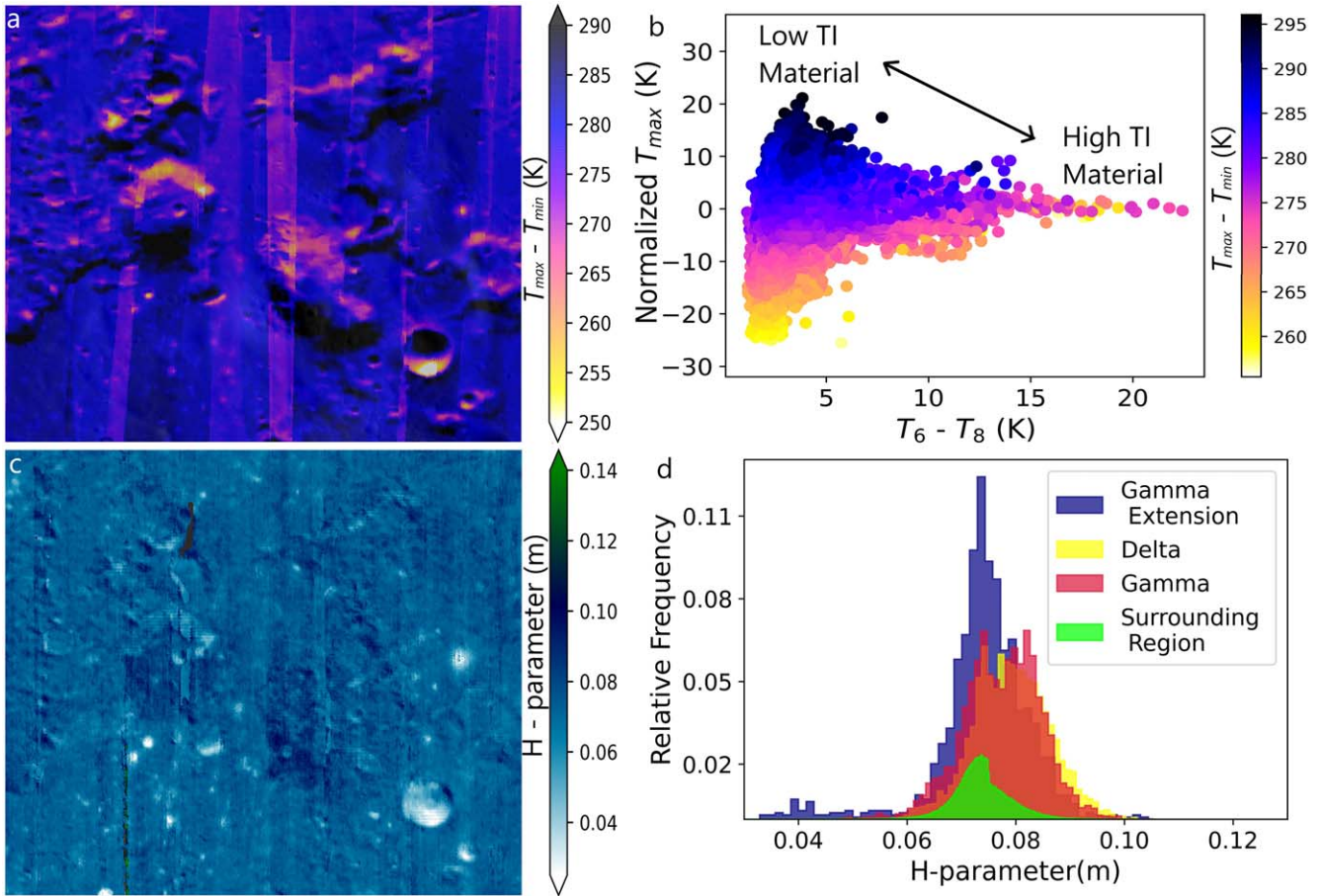The rock abundance map (Figure 10(a)) shows higher boulder abundances to the south of the Gamma dome, which

Figure 9. (a) Image displaying difference between the maximum and minimum temperatures in the region. (b) Normalized maximum temperature vs. nighttime anisothermality, with markers colored by temperature amplitude for pixels with slope less than 15°. (c) H-parameter map of the region. (d) Histogram displaying distribution of H-parameter across the domes for pixels with slope less than 15°.

Table 4
Median H-parameter and Maximum Rock Abundance of the Domes and Surrounding Regions

Name	Median H-parameter	Max Rock Abundance
Delta	0.08	0.9
Gamma	0.08	1.7
Gamma Extension	0.07	2.9
Surrounding Region	0.7	8.7

corresponds with the observed lower temperature difference amplitudes, lower H-parameter, and higher nighttime anisothermality (Figure 10(c)). We also observe a correlation between the rock abundance and nighttime anisothermality (Diviner channels 6 minus 8), resulting from a mixture of materials with differing thermophysical properties within the Diviner field of view (Figure 10(b)–(c)). These high anisothermality areas correspond to impact craters in the mare where blocky materials have been excavated by the impact process, demonstrating that the rock abundance model of Bandfield et al. (2011) is providing an appropriate interpretation of the Diviner nighttime anisothermality. Both the domes display high rock abundance near larger craters (Figure 10(a); however, the Gamma dome displays more craters on its top and higher anisothermality associated with them (Figures 10(b) and (c)).

Using LROC NAC images, we also mapped ~42,000 boulders on top of the Gamma dome, ranging from ~1 m to ~9 m (Figure 11(a)). Most of the rocks (~73% of mapped rocks) on top of the Gamma dome range between ~1–2 m in size (Figures 11(b)–(c)). These rocks in lower areal density and any potential stratification, like boulder 1 Station 2 from Apollo 17 (Ryder et al. 1975), can serve as time capsules to collect lunar samples from different geologic ages and events. We suspect that the drop in the frequency of boulders between 2 m and 1 m is due to a resolution effect. We used a power-law fit on the cumulative frequency–size distribution (Watkins et al. 2019) of the measured boulder lengths (Figure 11(d)) and observe the power-law index (b) to be −6.05, indicating complex fragmentation of rocks (Hartmann 1969). Hartmann (1969) specifies that the power-law index (b) or slope of the plot varies with the condition of fragmentation, with lower values of b (<0.8) indicating simple fragmentation and larger values indicating complex fragmentation. Complex fragmentation indicates that the size of boulders we see as of now is a result of breakdown due to additional factors such as micrometeoroid bombardment and thermal cycling after being shattered upon initial impact event. We suspect that the kink near 7.5–8 m in the data set could be potentially due to binning or mapping bias and errors.

We then compared our boulder map to the Diviner rock abundance and H-parameter maps (Figures 12(a)–(d)). We observe that elevated Diviner rock abundance values occur in
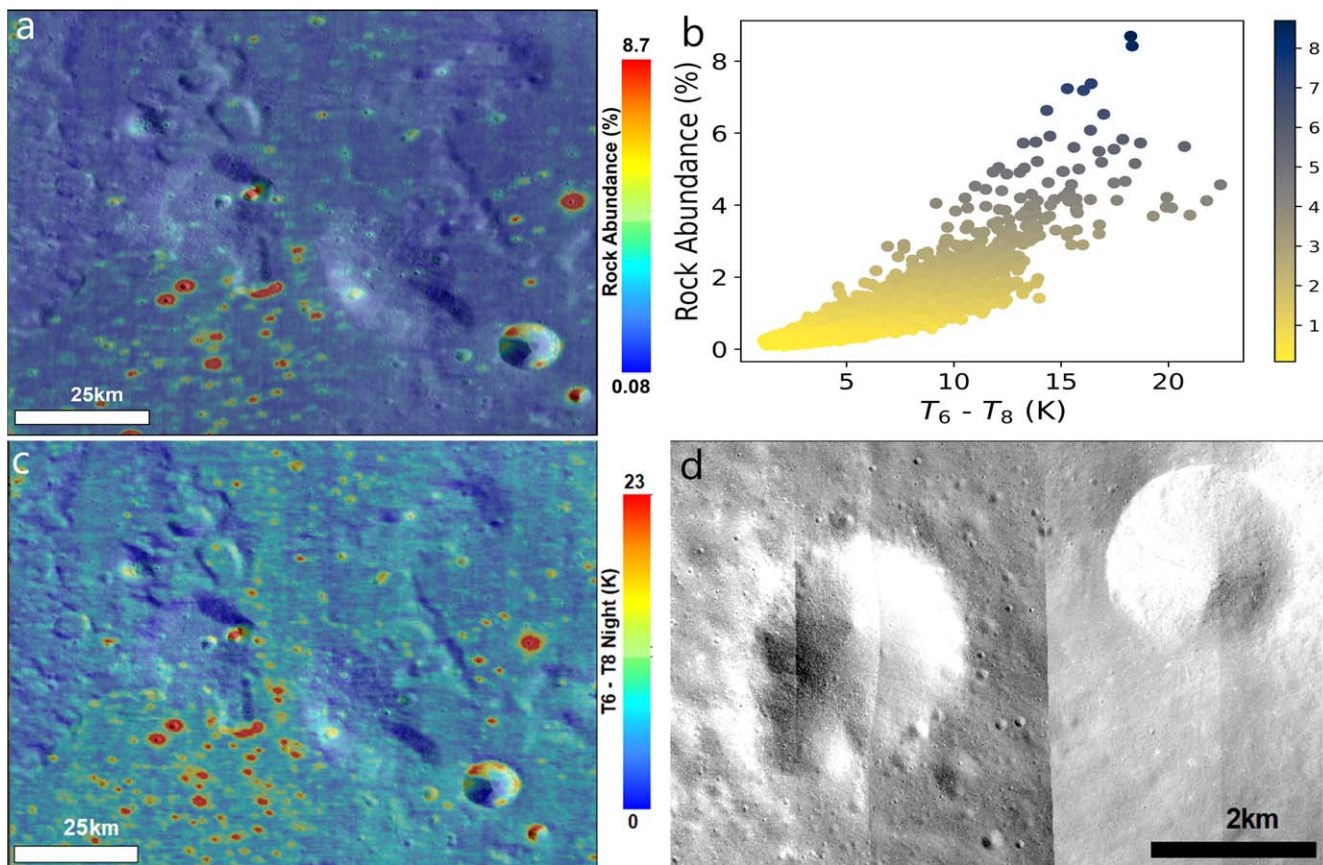
Figure 10. (a) Rock abundance map from Bandfield et al. (2017) of the region. (b) Rock abundance vs. nighttime anisothermality of the region (c) Nighttime anisothermality map of the region. (d) High-resolution NAC image of the two young craters atop the Gamma dome.

the regions where most of the rocks are larger than ~2 m (Figure 11(b)). Areas with a high density of rocks with smaller sizes do not register as high rock abundance values from Diviner measurements. However, these regions display lower H-parameter. Thus, H-parameter values might be sensitive to smaller rocks and therefore may be a better indicator of rock density at submeter scale on the domes. This is consistent with recent rock abundance comparisons conducted by Powell et al. (2023), who found that manual rock abundance estimates were consistent with Diviner-derived rock abundance estimated for boulder lengths >2 m, but Diviner rock abundance began underestimating rock abundance when including boulders at smaller sizes as hypothesized by Hayne et al. (2017). Both of the two large craters on the Gamma dome have elevated boulder counts in Figure 11(a) but only the easternmost displays higher rock abundance and low H-parameters (Figures 12(a) and (b)) from Diviner data. The morphology of the western crater also looks much more muted in LROC images (Figure 10(d)), so we suspect that the easternmost impact on the Gamma dome is younger and post-dates the other, as it displays both a fresher morphology and distinct thermophysical signature.

5. Discussion

Our compositional analysis indicates that the surrounding highlands region in which the Gamma and NW are partly located appears slightly mafic due to ejecta from craters in the mare region. Previous studies (e.g., Ivanov et al. 2016) focused on morphological mapping suggested that the Gamma extension is a remnant of underlying highlands material because of overlapping flow features of Gamma dome on top of the extension. We also could not identify any craters excavating silicic materials with low-CF values on the Gamma extension, despite low FeO content, consistent with it being of highland origin.

Recent studies (Kiefer et al. 2016; Qiu et al. 2023) have identified remnant magma chambers that are potentially of silicic nature beneath the Gruithuisen domes region. Qiu et al. (2023) carried out a 3D density anomaly inversion and identified low-density masses (100–200 kg m^{-3} lower than the average lunar crust density of 2550 kg m^{-3} (Kiefer et al. 2016)) beneath the domes. They further explain that, since the density of the lunar crust increases with depth due to decrease in porosity (Besserer et al. 2014), these anomalies are caused by presence of low-density masses, which aligns well with the density of silicic magma. Our study identified a new dome and a young crater excavating silicic material in the nearby region; hence it is possible that these chambers had several other smaller vents extruding silicic magmas in the nearby regions that were then blanketed by the ejecta from later impacts. The newly identified crater and dome have CF values well below (<7.4 μm) those of the feldspathic highlands (~7.8–8 μm) as well as lower FeO content (<7wt.% comparable to the highlands), indicating they are a separate unit. The young crater being superposed on the interior of an older crater (Figures 13(a)–(c)) may have enabled the impact to puncture through the regolith layer, making the excavation of silicic
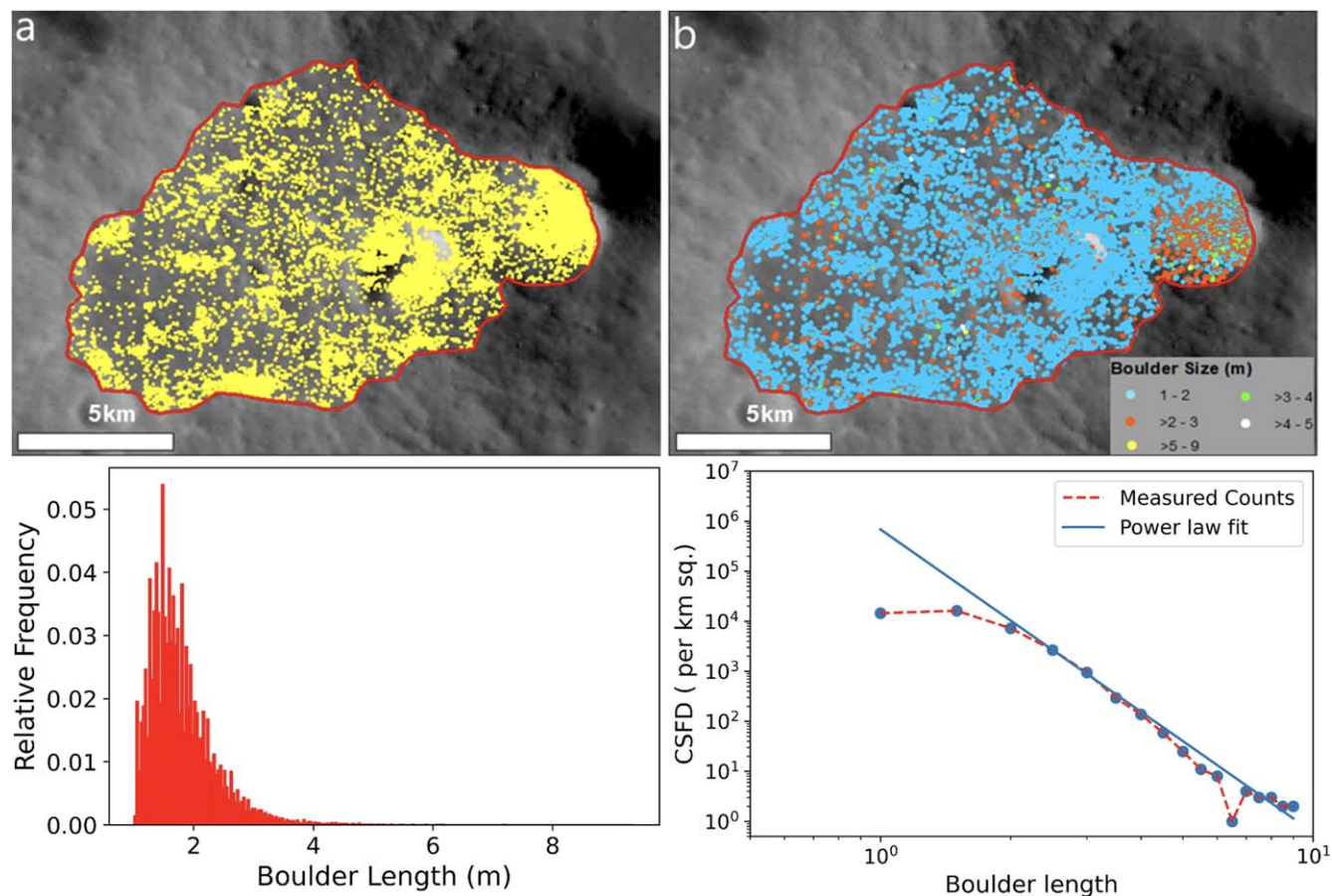
Figure 11. (a) Rocks mapped on top of the Gamma dome. (b) Map displaying the sizes of the mapped boulders atop the Gamma dome. (c) Histogram displaying boulder size on top of the Gamma dome. (d) Power-law fit between cumulative size frequency distribution and boulder lengths binned at 0.5 m intervals.

material more favorable. It is possible that the extent of the new dome and its associated silicic materials may be larger. We do not observe any clear morphological boundary between the dome and surrounding region from the NAC images (Figures 13(d)–(f)). The surrounding margins may appear mafic due to overlying material, possibly ejecta from the adjacent mare, while the silicic material may have remained exposed on the dome due to the higher elevation and slopes of the summit and its flanks.

The magnetic field strength data (Richmond & Hood 2008; Ravat et al. 2020) indicates the presence of a weak magnetic field to the north of the domes (Figure 14). The surface field model shown here is downward continued from orbital data and represents a lower bound on the possible surface field strength (e.g., Waller et al. 2022). Several studies (e.g., Kramer et al. 2011; Li & Garrick-Bethell 2019) indicate that regions with strong magnetic field display a depletion in OH and reduction in equilibrium of water abundance. Magnetic fields lead to deflection and thus reduction of solar wind protons—the primary source for hydrogen implantation in the lunar soil (Liu et al. 2012). Despite the presence of the weak magnetic field (at the lower end of measurement; see Section 2), we do not observe any localized decrease in the estimated water abundance (Figures 3(a) and (b)) in the region (e.g., Li & Garrick-Bethell 2019). This might indicate that the water abundance observed in the area is due to an endogenic source such as water-bearing volcanic rocks/regolith or pyroclastic

deposits (e.g., Ivanov et al. 2016) rather than exogenous water formed as a result of solar wind interaction with the lunar surface.

Our compositional and thermophysical study of the region confirms the presence of spatially extensive silicic volcanism in the Gruithuisen region area. These will aid in understanding the in situ context of silicic volcanism on the Moon. The exploration of this region will help in answering questions related to (1) the composition in terms of SiO_2 content; (2) the domes' formation in the absence of plate tectonics; (3) the spatial and temporal extent of silicic volcanism on the Moon; (4) potential volatiles present in lunar mantle through observation of pyroclastic deposits; (5) the spatial, compositional, and temporal relationships between the domes, the Gamma extension, and nearby mare, and (6) the thermal history and evolution of the Moon over time (e.g., Jolliff et al. 1999; Hagerty et al. 2006; Glotch et al. 2010; Ivanov et al. 2016).

The chosen landing site for Lunar-VISE (Williams et al. 2024) atop the Gamma dome near the young crater will serve as a useful site for deciphering the enigma of silicic non-mare volcanism on the lunar surface.

6. Summary

We have carried out a detailed characterization of the Gruithuisen region of the Moon using available remote sensing data. We find that the region hosts highly silicic domes amidst
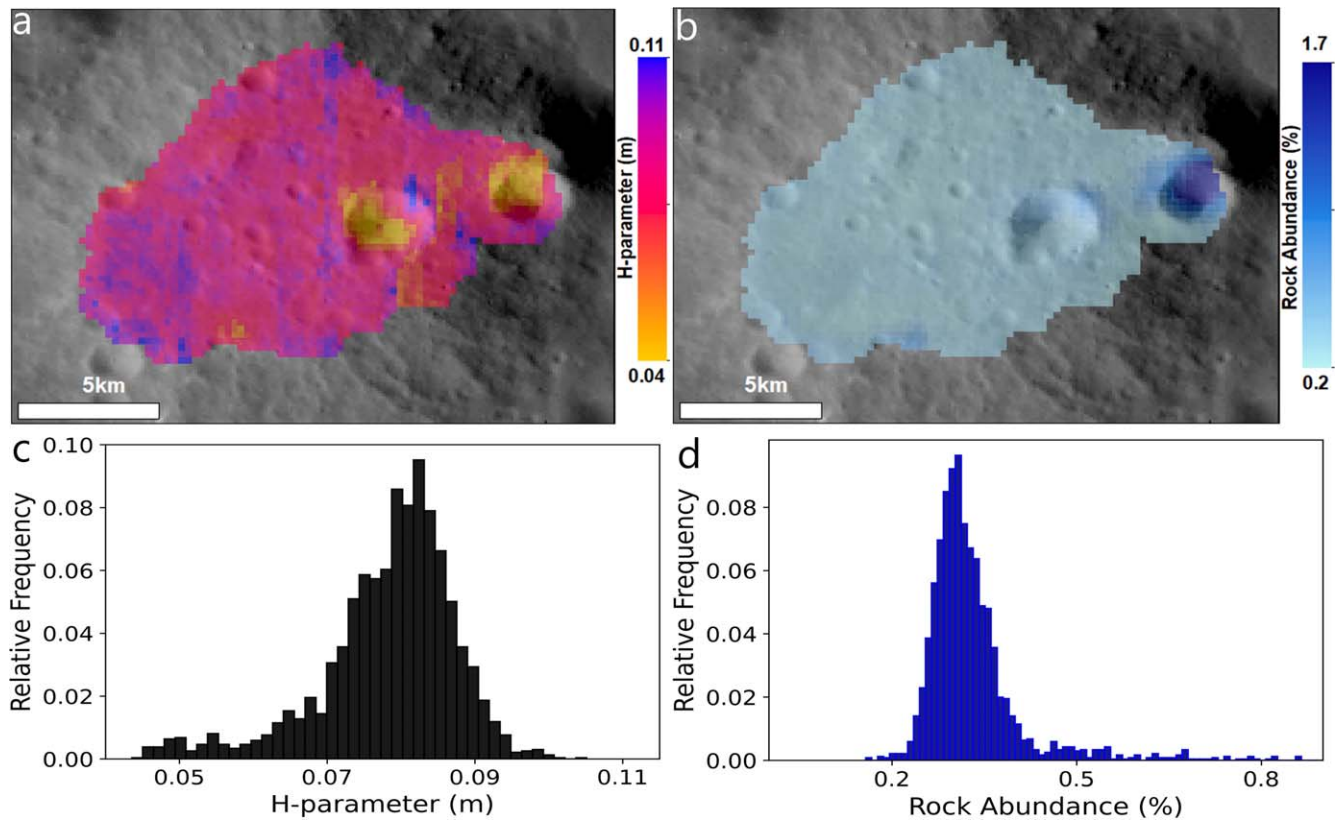
Figure 12. (a) H-parameter on top of the Gamma dome. (b) Rock abundance on top of the Gamma dome. (c) H-parameter on top of the Gamma dome. (d) Rock abundance on top of the Gamma dome.
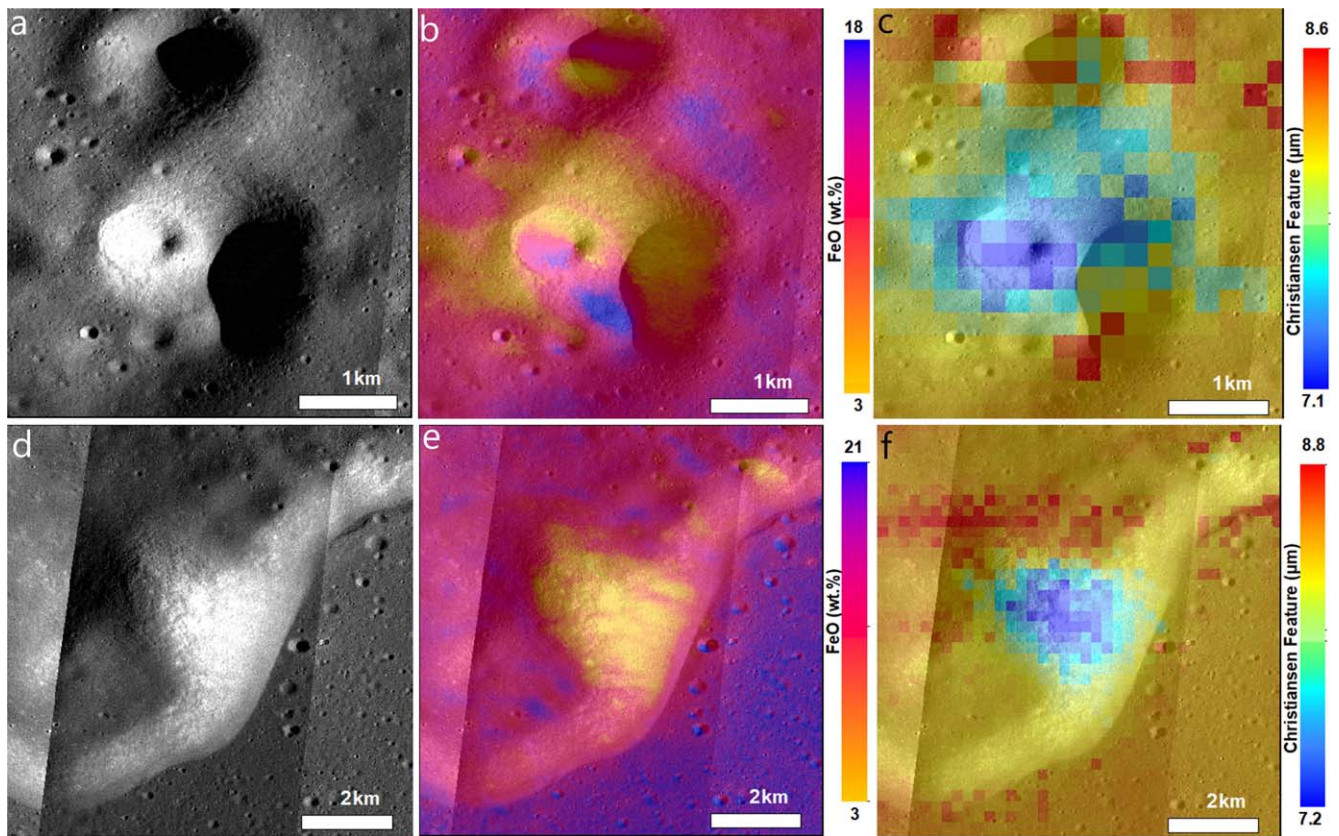

Figure 13. (a) NAC image of the newly identified crater. (b) FeO image of the crater. (c) CF image of the crater. (d) NAC image of the newly identified dome. (e) FeO image of the dome. (f) CF image of the dome.
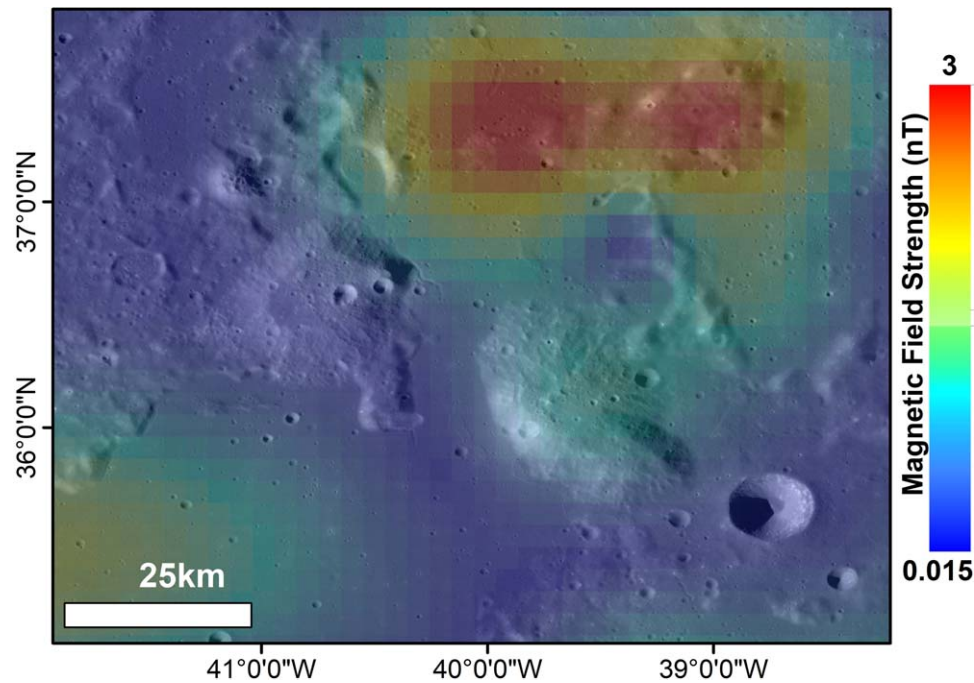
Figure 14. Magnetic field strength image of the region.

low-titanium basaltic lava flows. We have also identified additional areas of silicic nature nearby, including a possible fourth dome, suggesting that the silicic volcanism might have been more widespread in the area. Water abundance, despite a weak magnetic field anomaly, indicates that the observed water is endogenous and probably held by pyroclastics. The presence of potential pyroclastic in the area is consistent with the H-parameter maps and gravity data. The power-law index from the boulder counts indicates a complex fragmentation of rocks on the Gamma dome. The daytime temperature of the region is heavily influenced by the slopes and albedo, and the nighttime temperature is sensitive to thermophysical properties, with variations in anisothermality caused by the distribution of rocks. The in situ exploration of the region will substantially advance the understanding of the thermal and compositional evolution of the lunar surface.

Appendix

Table A1 displays 24 hr temperature variation on the domes and surrounding regions.

Table A1
24 hr Temperature Variation (Percentile) on the Domes and Surrounding Regions

Local Time	Gamma Temperatures (K)			Delta Temperatures (K)			Gamma Extension Temperatures (K)			Surrounding Region Temperatures (K)		
	25th	50th	Max	25th	50th	Max	25th	50th	Max	25th	50th	Max
1	95	96	100	95	96	100	95	95	114	95	96	119
2	93	94	97	93	94	99	93	94	109	94	94	109
3	92	93	97	91	92	96	92	92	107	92	93	114
4	90	91	95	90	91	95	90	91	106	91	91	104
5	90	91	95	90	90	95	90	91	108	90	91	114
6	89	90	93	89	90	93	89	90	104	89	90	126
7	185	210	296	113	128	301	192	243	293	190	211	295
8	262	270	311	185	203	318	269	280	309	263	269	328
9	314	320	356	297	306	350	321	324	352	318	321	357
10	332	338	362	313	320	360	344	247	363	336	339	364
11	356	361	376	351	354	379	361	363	377	359	362	380
12	359	364	379	353	357	382	366	367	376	364	366	383
13	357	363	381	358	361	379	359	361	373	363	365	381
14	356	361	379	357	361	378	348	351	365	354	358	384
15	332	338	359	347	350	367	338	342	358	342	345	365
16	309	314	344	315	323	343	298	307	346	307	312	358
17	264	284	311	300	308	328	261	275	306	282	287	327
18	131	199	281	202	215	281	202	227	279	189	209	308
19	114	118	147	117	121	155	112	113	139	115	116	158
20	106	107	113	107	108	116	106	106	134	106	107	136
21	103	105	109	105	106	113	103	103	124	104	105	128
22	99	101	106	101	101	207	100	101	122	101	101	122
23	98	99	104	98	99	104	98	99	120	99	100	125
24	96	97	102	97	97	102	96	97	114	97	97	113

ORCID iDs

Nandita Kumari ● https://orcid.org/0000-0001-5960-0914
Timothy D. Glotch ● https://orcid.org/0000-0002-8187-3609
Jean-Pierre Williams ● https://orcid.org/0000-0003-4163-2760
Catherine M. Elder ● https://orcid.org/0000-0002-9993-8861
Benjamin D. Byron ● https://orcid.org/0000-0003-4435-0347

References

Anderson, A. T., Braziunas, T. F., Jacoby, J., & Smith, J. V. 1972, LPSC, 3, 819
Bandfield, J. L., Cahill, J. T. S., Carter, L. M., et al. 2017, Icar, 283, 282
Bandfield, J. L., Ghent, R. R., & Vasavada, A. R. 2011, JGRE, 116, E00H02
Besserer, J., Nimmo, F., & Wieczorek, M. A. 2014, GeoRL, 41, 5771
Bhattacharya, S., Lal, D., Chauhan, M., Chauhan, P., & Kumar, A. K. 2015, Icar, 260, 167
Byron, B. D., Elder, C. M., & Glotch, T. D. 2023, PSJ, 4, 182
Chappell, B. W., & White, A. J. R. 1974, Pacific Geology, 8, 173
Chevrel, S. D., Pinet, P. C., & Head, J. W. 1999, JGR, 104, 16515
Cloutis, E. A. 2002, JGRE, 107, 5039
Donaldson Hanna, K. L., Benavente, J., Bennett, K., et al. 2023, LPSC, 54, 2152
Glotch, T. D., Lucey, P. G., & Bandfield, J. L. 2010, Sci, 329, 1510
Greenhagen, B. T., Lucey, P. G., Bandfield, J. L., et al. 2011, LPSC, 42, 2679
Greenhagen, B. T., Lucey, P. G., & Wyatt, M. B. 2010, Sci, 329, 1507
Hagerty, J. J., Lawrence, D. J., & Hawke, B. R. 2006, JGRE, 111, E06002
Hartmann, W. K. 1969, Icar, 10, 201
Haskin, L. A., Gillis, J. J., Korotev, R. L., & Jolliff, B. L. 2000, JGR, 105, 20403
Hayne, P. O., Bandfield, J. L., Siegler, M. A., et al. 2017, JGRE, 122, 2371
Head, J. W., III, & McCord, T. B. 1978, Sci, 199, 1433
Hemingway, D. J., & Tikoo, S. M. 2018, JGRE, 123, 2223
Henderson, B. G., & Jakosky, B. M. 1997, JGR, 102, 6567
Hendrix, A. R., Hurley, D. M., Farrell, W. M., et al. 2019, GeoRL, 46, 2417
Ivanov, M. A., Head, J. W., & Bystrov, A. 2016, Icar, 273, 262
Jolliff, B. L. 1991, LPSC, 21, 101

Jolliff, B. L., Floss, C., McCallum, I. S., & Schwartz, J. M. 1999, AmMin, 84, 821
Jolliff, B. L., Gillis, J. J., Haskin, L. A., Korotev, R. L., & Wieczorek, M. A. 2000, JGR, 105, 4197
Kiefer, W. S., Taylor, G. J., Andrews-Hanna, J. C., et al. 2016, LPSC, 47, 1722
Klima, R. L., Dyar, M. D., & Pieters, C. M. 2011, M&PS, 46, 379
Klima, R. L., Pieters, C. M., & Dyar, M. D. 2007, M&PS, 42, 235
Klima, R. L., Pieters, C. M., & Dyar, M. D. 2008, M&PS, 43, 1591
Kneissl, T., van Gasselt, S., & Neukum, G. 2011, P&SS, 59, 1243
Kramer, G. Y., Besse, S., Dhingra, D., et al. 2011, JGRE, 116, E00G04
Kusuma, K. N., Sebastian, N., & Murty, S. V. S. 2012, P&SS, 67, 46
Lemelin, M., Lucey, P. G., Gaddis, L. R., Hare, T., & Ohtake, M. 2016, LPSC, 47, 2994
Li, S., & Garrick-Bethell, I. 2019, GeoRL, 46, 14318
Li, S., & Milliken, R. E. 2017, SciA, 3, e1701471
Liu, Y., Guan, Y., Zhang, Y., et al. 2012, NatGe, 5, 779
Loiselle, M. C., & Wones, D. S. 1979, Geological Society of America, Abstracts with Programs, 11, 468
Lucey, P. G., Blewett, D. T., & Jolliff, B. L. 2000, JGR, 105, 20297
Meyer, C., Williams, I. S., & Compston, W. 1996, M&PS, 31, 370
Milliken, R. E., & Li, S. 2017, NatGe, 10, 561
Moriarty Iii, D. P., & Pieters, C. M. 2018, JGRE, 123, 729
Ohtake, M., Haruyama, J., Matsunaga, T., et al. 2008, EP&S, 60, 257
Paige, D. A., Foote, M. C., Greenhagen, B. T., et al. 2009, SSRv, 150, 125
Papike, J. J., Ryder, G., & Shearer, C. K. 1998, in Planetary Materials, Vol. 36, ed. J. J. Papike (Chantilly, VA: Mineralogical Society of America), 5–001
Powell, T. M., Horvath, T., Lopez Robles, V., et al. 2023, JGRE, 128, e2022JE007532
Purucker, M. E., & Nicholas, J. B. 2010, JGRE, 115, E12007
Qiu, D., Sasaki, S., Yan, J., et al. 2023, GeoRL, 50, e2023GL103336
Ravat, D., Purucker, M. E., & Olsen, N. 2020, JGRE, 125, e06187
Richmond, N. C., & Hood, L. L. 2008, JGRE, 113, E02010
Robinson, M. S., Brylow, S. M., & Tschimmel, M. E. 2010, SSRv, 150, 81
Roedder, E., & Weiblen, P. W. 1970, in Mineralogy and Petrology, Vol. 1, ed. A. A. Levinson (New York: Pergammon Press), 801
Ryder, G. 1976, E&PSL, 29, 255
Ryder, G. R., Stoeser, D. B., Marvin, U. B., & Bower, J. F. 1975, LPSC, 6, 435
Seddio, S. M., Jolliff, B. L., Korotev, R. L., & Zeigler, R. A. 2013, AmMin, 98, 1697
Seddio, S. M., Korotev, R. L., Jolliff, B. L., & Wang, A. 2015, AmMin, 100, 1533

Thornton, C. P., & Tuttle, O. F. 1960, AmJS, 258, 664

Tsunakawa, H., Takahashi, F., Shimizu, H., Shibuya, H., & Matsushima, M. 2015, JGRE, 120, 1160

Wagner, R., Head, J. W., Wolf, U., & Neukum, G. 2002, JGRE, 107, 5104

Waller, C. D., Cahill, J. T. S., Retherford, K. D., et al. 2022, FrASS, 9, 926018

Watkins, R. N., Jolliff, B. L., Mistick, K., et al. 2019, JGRE, 124, 2754

Whitaker, E. A. 1972, Moon, 4, 348

Whitney, J. A. 1988, GSAB, 100, 1886

Williams, J. P., Greenhagen, B. T., Bennett, K. A., et al. 2022, E&SS, 9, e01966

Williams, J. P., Landis, M., Bennett, K., et al. 2024, LPSC, 55, 1688

Williams, J. P., Paige, D. A., Greenhagen, B. T., & Sefton-Nash, E. 2017, Icar, 283, 300

Wilson, L., & Head, J. W. 2003, GeoRL, 30, 1605

Xiao, X., Yu, S., Huang, J., et al. 2022, Natl. Sci. Rev., 9, nwac175

Yang, J., Ju, D., & Pang, R. 2023, GeCoA, 340, 189